Electronic Supplementary Material (ESI) for CrystEngComm.


# SUPPORTING INFORMATION

## A H-shaped heterometallic $Sn_4Au_4$ system with guest-tuneable multicolour and selective luminescence sensing properties

Csaba Jobbágy,[a] Péter Baranyai,[a§] Ágnes Gömöry[b] and Andrea Deák*[a]

[a] Hungarian Academy of Sciences, MTA TTK SZKI,
"Lendület" Supramolecular Chemistry Research Group,
1117 Budapest, Magyar Tudósok körútja 2, Hungary
E-mail: deak.andrea@ttk.mta.hu

[b] Hungarian Academy of Sciences, MTA TTK SZKI,
MS Proteomics Research Group,
1117 Budapest, Magyar Tudósok körútja 2, Hungary

[§] Present address: Institute for Solid State Physics and Optics,
Wigner Research Centre for Physics of the Hungarian Academy of Sciences,
Department of Applied and Nonlinear Optics,
1121 Budapest, Konkoly-Thege Miklós út 29-33, Hungary

## Experimental Section

### 1. General procedures and physical measurements

All chemicals and solvents used for the syntheses were of reagent grade. The solvents for synthesis were used without further purification. All manipulations were performed in air. The elemental analysis has been carried out with an Elementar Vario EL III apparatus.
Infrared spectrum was recorded in the 400 to 4000 $cm^{-1}$ spectral range on a Varian 2000 FT-IR spectrometer equipped with Golden Gate single reflection diamond ATR (Specac Ltd.).
NMR experiments were carried out on Varian Inova (400 MHz for $^{1}H$) spectrometer using an inverse detection two-channel pfg 5mm $^{1}H\{X\}$ probe (X = $^{31}P$, $^{119}Sn$). Samples were measured in a 5 mm NMR tube at 25 °C. $^{1}H$ chemical shifts are referenced to the residual solvent signal ($CD_2Cl_2$: 5.32 ppm). $^{31}P$ and $^{119}Sn$ shifts are given relative to the external reference 85% $H_3PO_4$ and $Me_4Sn$ (0.00 ppm) signal, respectively. $^{1}H$ spectra were recorded with 16 seconds, while the $^{31}P$ spectra with 12 seconds and the $^{119}Sn$ spectra with 3 seconds relaxation delay and WALTZ-16 proton decoupling. Deuterated (99.98 atom%) solvent was purchased from Cambridge Isotope Laboratories, Inc. The mass spectrometric measurements were performed using a Q-TOF Premier mass spectrometer (Waters Corporation, 34 Maple St, Milford, MA, USA) in positive electrospray mode. The UV–Vis absorption spectra in solution phase were measured on an Agilent 8452A photodiode array spectrometer. Steady state and time-resolved luminescence measurements were carried out on an Edinburgh Instrument FLSP920 spectrofluorimeter. Spectral corrections were applied using excitation and emission correction functions of the instrument. Longpass filters were used to exclude the scattered excitation light. The solid-state luminescence measurements at low-temperature (77 K) were recorded in a quartz capillary tube immersed in liquid nitrogen. The excitation light source was a μF900H xenon flashlamp (pulse duration: 2 μs at FWHM) or EPL-375 diode laser (pulse duration: 100 ps at FWHM) for the luminescent lifetime measurements. Solutions were deoxygenated by bubbling high purity $N_2$ for 15 minutes before lifetime measurements. In solid state, the absolute measurements of photoluminescence quantum yields were determined in a calibrated integrating sphere with Spectralon inner surface coating.
The adsorption isotherms for $N_2$ gas was measured by static volumetric method using fully automated Autosorb 1C (Quantachrome) equipment. Prior to analysis the sample was heated and kept at 25 °C under vacuum for 24 hours to remove all the previously adsorbed gases from the surface. The measurement was carried out at 77 K.
In the present study density functional theory (DFT) and time-dependent density functional theory (TD DFT) calculations were performed by using the *Gaussian 09* program package[1] at the PBE0/6-31G* level of theory. Relativistic effects were included for the Sn and Au atoms by using the Los Alamos National Laboratory double zeta type (LANL2DZ) pseudopotential. The geometries of the ground state of Hdppba ligand, metalloligand **1** and heterometallic **2** were fully optimized in the gas phase without symmetry constraints and vibrational frequency calculations were performed to verify that the optimized structures are minima on the potential energy surface. After geometry optimization the excited states were investigated by TD DFT analysis. The absorption wavelengths and oscillator strengths were obtained by TD DFT method at the optimized ground state geometry using the same functional and basis sets as for geometry optimization. Absorption spectra were simulated by GaussSum 3.0 software.[2] The molecular orbital surfaces were plotted by Molekel 5.4 visualization software at an isosurface value of 0.03 au.[3]
LINKAM Imaging Station microscope equipped with Nikon DS-Fi1c digital camera was used for digital recording.

## 2. Synthesis and characterisation

All reagents were used as received. The synthesis of metalloligand **1** and its heterometallic $Sn_4Au_4$ molecular clip **2** are shown in Scheme S1 followed by synthetic procedures and their characterization data.

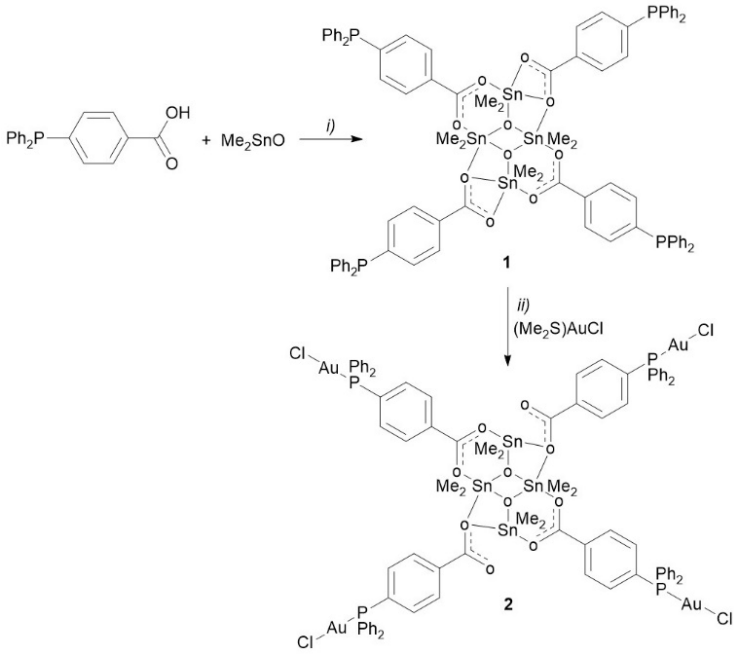


**Scheme S1** Synthesis of **1** and **2**.

**Synthesis of 1:** A solution of Hdppba (0.612 g, 0.2 mmol) in 5 mL ethanol was added to a suspension of $Me_2SnO$ (0.330 g, 0.2 mmol) in 5 mL ethanol. The reaction mixture was heated under refluxed for 3 hours. The resulting white solid was filtered off and dissolved in dichloromethane. *n*-hexane was added to precipitate a white microcrystalline solid. The obtained solid was purified by recrystallizations ($CH_2Cl_2$/*n*-hexane, 2:1) and washing with small portions of dichloromethane to give **1** as a white solid (0.540 g, 58 %). M.p. 210 °C; Diffraction quality single crystals were obtained by vapour diffusion of *n*-hexane into a dichloromethane solution. IR data: 3328 (w, br), 3191 (w, br), 3054 (m), 2924 (w), 1595 (s), 1534 (s), 1479 (m), 1434 (m), 1395 (s), 1360 (s), 1302 (m), 1180 (w), 1091 (w), 1017 (w), 999 (w), 859 (w), 772 (m), 743 (m), 726 (s), 693 (s), 579 (w), 511 (w); NMR data: $^{1}$H NMR (400 MHz, $CD_2Cl_2$, 25 °C): δ 7.89 (d, $J$ = 7.8 Hz, 8H), 7.37 – 7.30 (m, 48H) 0.95 (s, $^{2}J(^{119}Sn/^{117}Sn\text{-}^{1}H)$ = 90.0 Hz, 12H), 0.89 (s, $^{2}J(^{119}Sn/^{117}Sn\text{-}^{1}H)$ = 86.7 Hz, 12H); $^{31}P/\{^{1}H\}$ NMR (400 MHz, $CD_2Cl_2$, 25 °C): δ 27.1 (s), -5.4 (s, 4P); $^{119}Sn/\{^{1}H\}$ NMR (400 MHz, $CD_2Cl_2$, 25 °C): δ -180.9 (broad, $^{2}J(^{119}Sn\text{-}^{117}Sn/^{119}Sn)$ unresolved), -192,8 (broad, $^{2}J(^{119}Sn\text{-}^{117}Sn/^{119}Sn)$ unresolved) ppm.

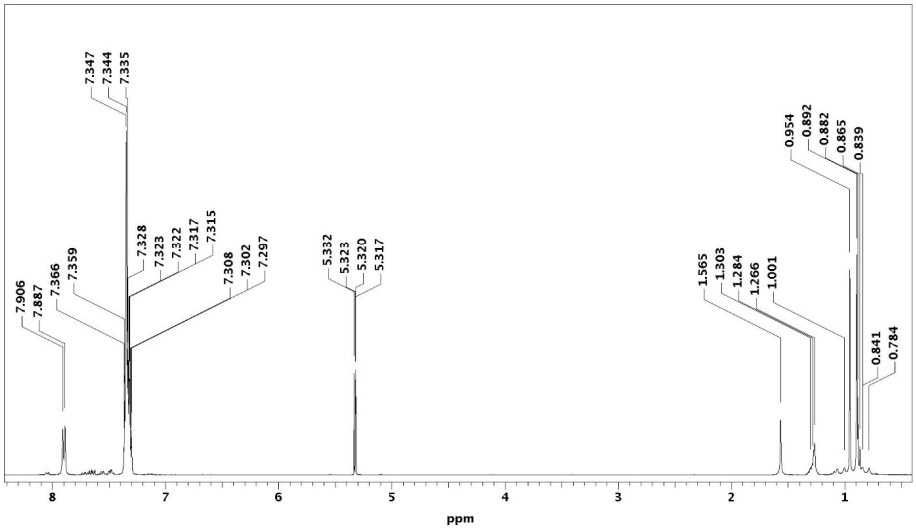


**Fig. S1** $^{1}$H-NMR spectrum of **1**.

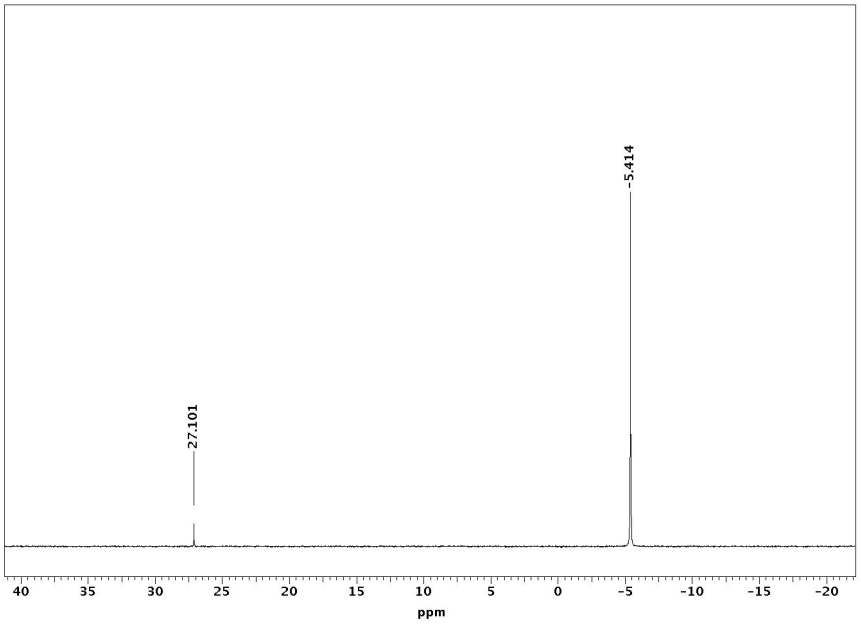


**Fig. S2** $^{31}$P-NMR spectrum of **1**.

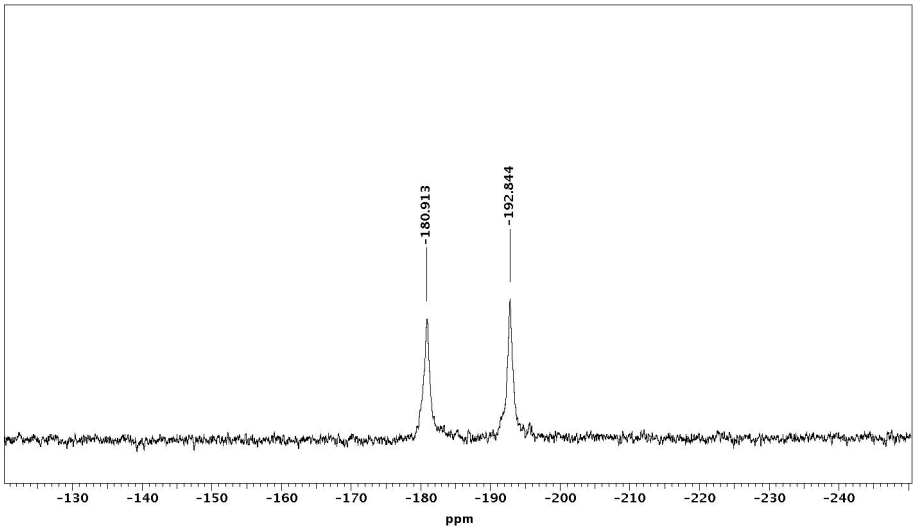


**Fig. S3** $^{119}$Sn-NMR spectrum of **1**.

The $^{31}$P NMR spectrum (Fig. S2) displays two sharp singlets at –5.4 ppm and a peak at 27.1 ppm. The former peak is comparable to that of free phosphine ligand (δ = –4.8 ppm). The $^{119}$Sn NMR spectrum (Fig. S3) recorded in $d_2$-$CH_2Cl_2$ shows the presence of two peaks at δ = –180.9 and –192.8 ppm characteristic of tetranuclear $\{[Me_2Sn(RCOO)]_2O\}_2$ organostannoxanes.[4] The presence of fully oxidized form of the dppba was also observed in the $^{31}$P NMR spectrum of hexameric $[^nBuSn(dppba)O]_6$ organostannoxanne.[5]

To asses the origin of the later peak, we used the procedure reported by Chandrasekhar,[5] and oxidized **1** with $H_2O_2$ to generate the anticipated oxidized phosphine groups. Complex **1** (0.092 g, 0.05 mmol) and large excess of hydrogen peroxide (200 µL) were stirred in dichloromethane for 4 hours. The colourless solution was filtered through Celite and *n*-hexane was added to precipitate the white microcrystalline complex. This solid was identified as $\{[Me_2Sn(dppOba)]_2O\}_2$ (**1O**) (dppOba = 4-$Ph_2P(O)$-$C_6H_4$-$CO_2$). The $^{31}$P NMR spectrum (Fig. S4) of this **1O** complex displays a singlet at 27.0 ppm, similar to that observed for **1**. This suggests that along with **1** the **1O** complex with oxidized phosphine groups in the periphery was formed as a side product. However, any attempts to isolate **1** in its pure form were unsuccessful, which is also reflected in the elemental analysis data. Elemental analysis calcd (%) for **1**·1.23 $CH_2Cl_2$: C 52.42, H 4.26; found: C 50.60, H 4.42.

As for other organotin(IV) complexes containing multiple tin atoms, the electrospray ionization mass spectrometry (ESI-MS) of **1** and **2** shows the presence of fragment ions, however, the corresponding molecular ion is not observed in the spectra.[6]

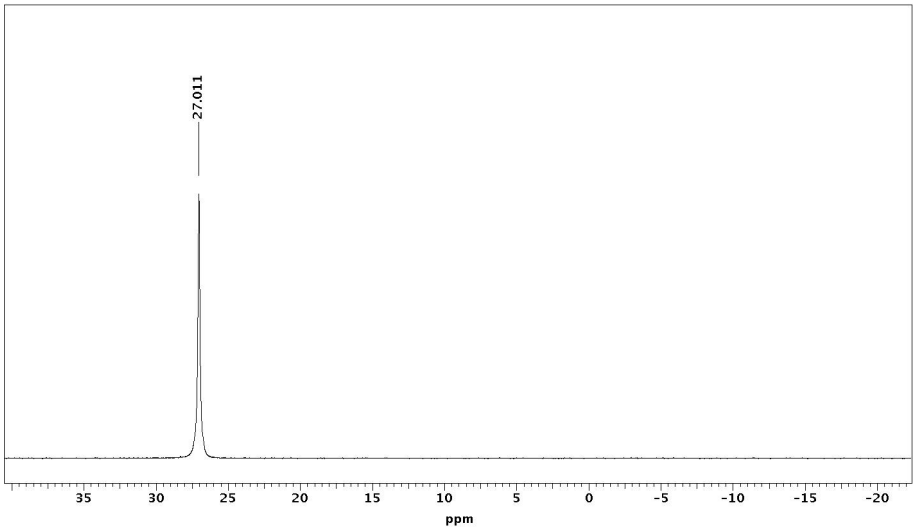


**Fig. S4** $^{31}$P-NMR spectrum of **1O**.

**Synthesis of 2:** A solution of **1** (0.231 g, 0.125 mmol) in 5 mL dichloromethane was added to a solution of ($Me_2S$)AuCl (0.147 g, 0.5 mmol) in 5 mL dichloromethane. After 5 hours of stirring shielded from light, diethyl ether was added and crystals of **2** were obtained overnight by slow evaporation of this solution. The crystals were filtered off, washed with small portions of dichloromethane and diethyl ether (215 mg, 62 %). M.p. >175 °C (decomp.);. Diffraction quality single crystals were obtained by vapour diffusion of diethyl ether into a dichloromethane solution. Elemental analysis calcd (%) for **2**·3.88 $CH_2Cl_2$: C 33.97, H 2.85; found: C 33.73, H 2.85. IR data: 3054 (w), 2918 (w), 1649(m), 1586 (s), 1539 (s), 1482 (m), 1435 (s), 1391 (s), 1322 (s), 1300 (s), 1099 (s), 1184 (w), 1133 (w), 1015 (w), 999 (w), 849(w), 773 (m), 747 (w) 724 (w), 688 (m), 646 (m), 557(m), 530 (m); NMR data: $^1$H NMR (400 MHz, $CD_2Cl_2$, 25 °C): δ 8.05 (d, $J$ = 8.2 Hz, 8H), 7.62 – 7.48 (m, 48H), 0.97 (s, $^2J(^{119}Sn/^{117}Sn\text{-}^1H)$ = 87.0 Hz, 12H), 0.92 (s, $^2J(^{119}Sn/^{117}Sn\text{-}^1H)$ = 87.0 Hz, 12H); $^{31}$P/{$^1$H} NMR (400 MHz, $CD_2Cl_2$, 25 °C): δ 32.9 (s); $^{119}$Sn/{$^1$H} NMR (400 MHz, $CD_2Cl_2$, 25 °C): δ -174.8 (broad, $^2J(^{119}Sn\text{-}^{117}Sn/^{119}Sn)$ unresolved), -190.6 (broad, $^2J(^{119}Sn\text{-}^{117}Sn/^{119}Sn)$ unresolved) ppm.

There are no traces of fully oxidized form of the dppba in the $^{31}$P NMR spectrum of **2** (Fig. S6).

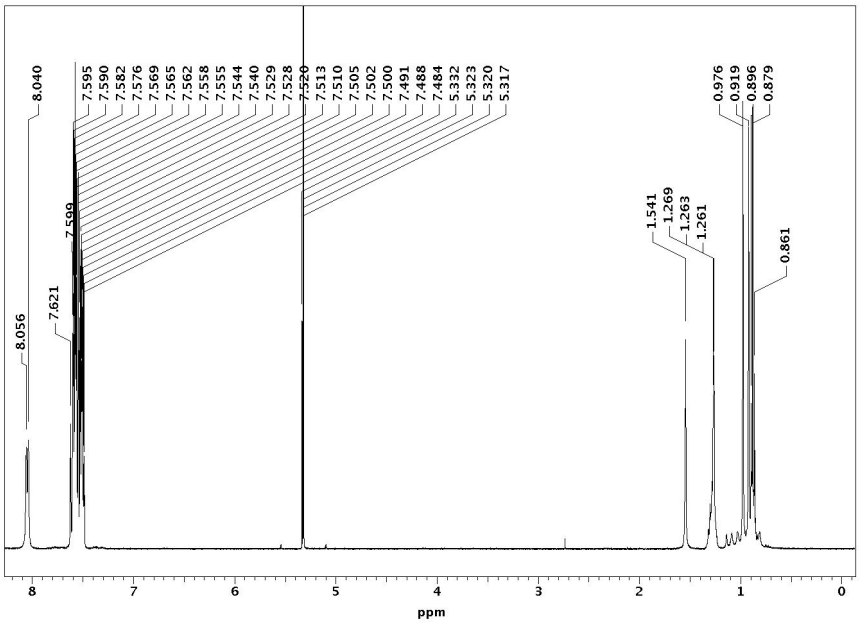


**Fig. S5** $^{1}$H-NMR spectrum of **2**.

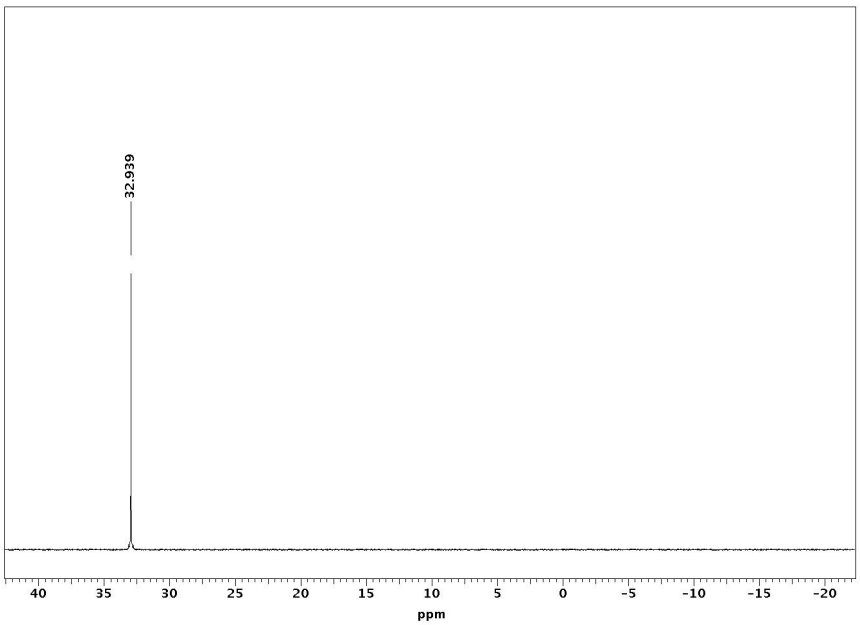


**Fig. S6** $^{31}$P-NMR spectrum of **2**.

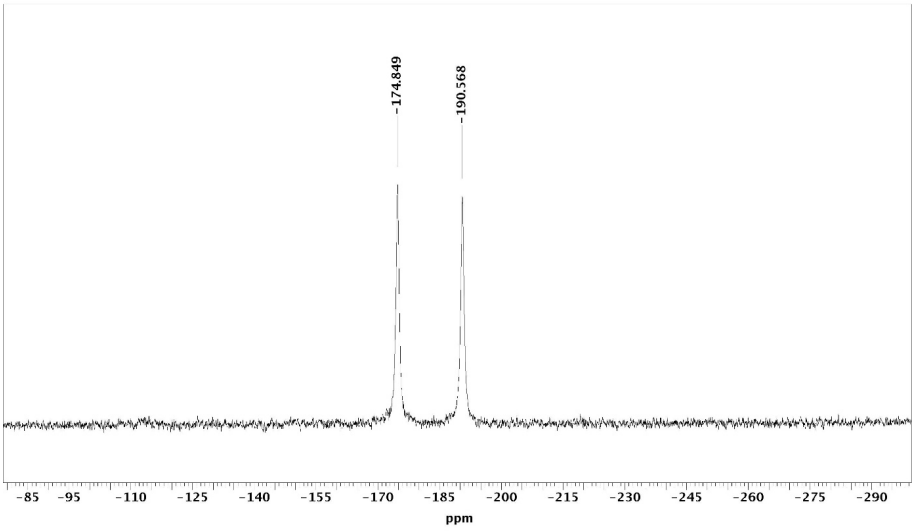


**Fig. S7** $^{119}$Sn-NMR spectrum of **2**.

The gas sorption behaviour of **2** and its permanent porosity was probed by standard procedures with $N_2$ at 77 K. The low BET surface area of 9.2 $m^2g^{-1}$ indicates that **2** is nonporous with regard to $N_2$ sorption (Fig. S8).

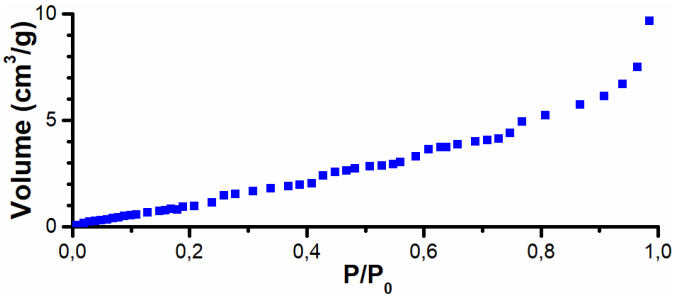


**Fig. S8** Adsorption isotherm for $N_2$ on **2** measured at 77K.

## 3. Single crystal X-ray diffraction

Crystals of **1**·1.23$CH_2Cl_2$ and **2**·3.88$CH_2Cl_2$ were mounted in Paratone-N oil within a conventional cryo-loop, and intensity data were collected on a Rigaku R-AXIS RAPID image plate diffractometer (λ(Mo-$K_\alpha$ radiation) = 0.71070 Å), fitted with an X-stream low temperature attachment. Several scans in the φ and ω direction were made to increase the number of redundant reflections, which were averaged over the refinement cycles. The structures were solved by direct method (*SIR*92)[7] and refined by full-matrix least-squares (*SHELXL*-2016).[8] All non-hydrogen atoms were refined anisotropically in $F^2$ mode. Hydrogen atomic positions were generated from assumed geometries. The riding model was applied for the hydrogen atoms. Only the methyl hydrogen atoms were refined as riding and rotating groups. In structure **1**·1.23$CH_2Cl_2$, residual electron density maximum of 3.651 eÅ$^{-3}$ and minimum of –1.561 eÅ$^{-3}$ were found close to adjacent Cl1 atom of a disordered dichloromethane molecule (1.50 Å from Cl1 and 0.63 Å from Cl1, respectively). Alternate positions for the Cl atom have been tried, but only the current structural model resulted in a reasonable geometry and stable refinement. Thus, the positive residual density maximum of 3.651 eÅ$^{-3}$ at (0.9867, 0.5356, 0.0390) is 1.50 Å from Cl1, 2.14 Å from Cl1$^{i}$ ($i$ = –x,1–y,–z), 2.38 Å from Cl2 and 2.42 Å from C19. The residual density minimum of –1.561 eÅ$^{-3}$ at (0.0385, 0.5918, 0.0391) is 0.63 Å from Cl1, 1.83 Å from C19, 2.26 Å from Cl2 and 2.37 Å from H19B. In **2**·3.88$CH_2Cl_2$, the positive residual density maximum of 2.033 eÅ$^{-3}$ at (0.1731, 0.3044, 0.3462) is 1.39 Å from H20A, 1.80 Å from Cl4, 2.08 Å from C20 and 2.12 Å from C19. The residual density minimum of –2.160 eÅ$^{-3}$ at (0.7074, 1.2012, 0.2998) is 0.84 Å from Au2, 1.56 Å from Cl2, 2.54 Å from H5A and 3.00 Å from P2.

**Table S1** Crystal data and structure refinement parameters for **1** and **2**, respectively.

| Complex | **1** | **2** |
|---|---|---|
| Formula | $C_{84}H_{80}O_{10}P_4Sn_4$ 1.226·($CH_2Cl_2$) | $C_{84}H_{80}Au_4Cl_4O_{10}P_4Sn_4$ 3.876·($CH_2Cl_2$) |
| Formula weight | 1952.21 | 3107.06 |
| Crystal size [mm] | 0.30 × 0.39 × 0.51 | 0.22 × 0.24 × 0.45 |
| Colour | colourless | colourless |
| Crystal system | triclinic | monoclinic |
| Space group | $P\ \bar{1}$ | $P2_1/c$ |
| Temp. (K) | 109(2) | 103(2) |
| $a$ [Å] | 8.5756(1) | 9.8918(10) |
| $b$ [Å] | 15.1244(2) | 14.2582(13) |
| $c$ [Å] | 18.2776(5) | 39.597(3) |
| $\alpha$ [°] | 112.516(1) | 90 |
| $\beta$ [°] | 99.834(4) | 93.948(2) |
| $\gamma$ [°] | 98.038(3) | 90 |
| $V$ [Å$^3$] | 2102.17(9) | 5571.5(9) |
| Z | 1 | 2 |
| $d_{calc}$ [Mg/m$^3$] | 1.542 | 1.852 |
| $\mu$ [mm$^{-1}$] | 1.384 | 6.495 |
| $F$(000) | 975 | 2942 |
| No. of collected reflns. | 65098 | 61589 |
| No. of indep. reflns./$R_{int}$ | 7412/0.040 | 6745/0.141 |
| No. of obsd. reflns. $I > 2\sigma(I)$ | 7157 | 5048 |
| No. of parameters | 492 | 566 |
| GOF | 1.09 | 1.07 |
| $R1$ (obsd. data) | 0.0403 | 0.0686 |
| $wR2$ (obsd. data) | 0.1091 | 0.1782 |
| Largest diff. peak/ hole (e Å$^{-3}$) | 3.65/–1.56 | 2.03/–2.16 |

**Table S2** Relevant bond lengths (Å) and angles (°) of **1** and **2**, respectively.

| | **1** | **2** |
|---|---|---|
| Sn(1)−O(1) | 2.185(3) | 2.178(2) |
| Sn(1)···O(2) | 2.799(3) | 2.921(3) |
| Sn(1)−O(4) | 2.280(3) | 2.296(3) |
| Sn(1)−O(5) | 2.017(3) | 2.019(2) |
| | | |
| Sn(2)···O(1) | 2.733(2) | 2.716(2) |
| Sn(2)−O(5) | 2.143(3) | 2.132(2) |
| Sn(2)−O(3)$^{i}$ | 2.247(3) | 2.251(2) |
| Sn(2)−O(5)$^{i}$ | 2.047(3) | 2.044(2) |
| | | |
| Sn(2)···Sn(2)$^{i}$ | 3.2852(4) | 3.2854(2) |
| | | |
| Au(1)–Cl(1) | | 2.293(5) |
| Au(2)–Cl(2) | | 2.283(6) |
| Au(1)–P(1) | | 2.225(5) |
| Au(2)–P(2) | | 2.224(6) |
| | | |
| Cl(1)–Au(1)–P(1) | | 176.6(2) |
| Cl(2)–Au(2)–P(2) | | 177.3(2) |
| | | |
| O(1)–Sn(1)−O(4) | 165.9(2) | 166.7(5) |
| O(1)–Sn(1)−O(5) | 79.3(2) | 79.2(5) |
| O(4)–Sn(1)−O(5) | 89.2(2) | 88.1(5) |
| C(15)–Sn(1)–C(16) | 141.3(2) | 137.5(8) |
| | | |
| O(5)–Sn(2)−O(3)$^{i}$ | 165.5(2) | 169.1(5) |
| O(5)–Sn(2)−O(5)$^{i}$ | 76.7(2) | 76.3(4) |
| O(1)–Sn(2)−O(3)$^{i}$ | 128.3(2) | 124.6(4) |
| O(1)–Sn(2)−O(5)$^{i}$ | 142.1(2) | 142.1(4) |
| C(17)–Sn(2)–C(18) | 147.0(2) | 148.3(8) |

wherein $i$ = –x, –y, 1–z (**1**) and $i$ = 1–x, 2–y, –z (**2**)

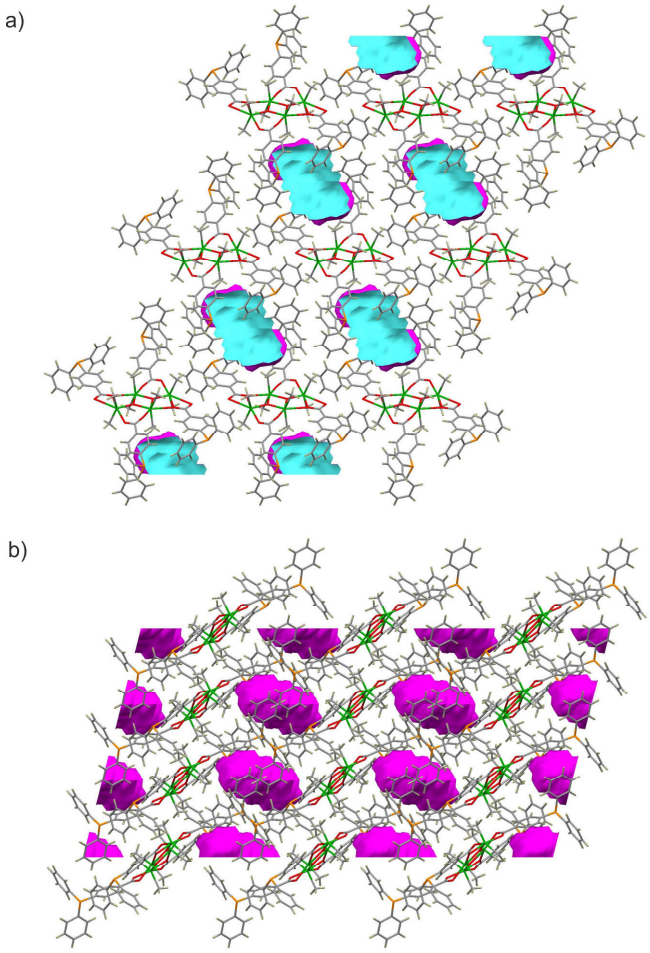


**Fig. S9** Packing arrangement of **1** showing the discrete voids (outside colour: magenta; inside colour: ice blue) hosting the dichloromethane molecules viewed along the crystallographic a) *a* and b) *b* axis, respectively. The solvent molecules are omitted for the sake of clarity.

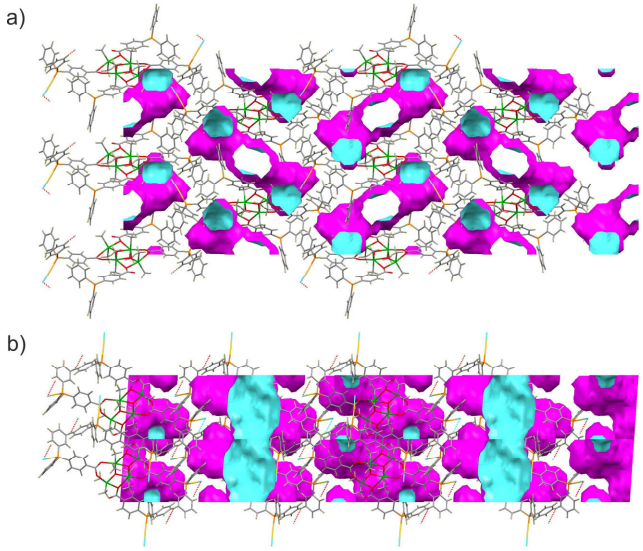


**Fig. S10** Packing arrangement of **2** showing the channels having large dumbbell-shaped cavities (outside colour: magenta; inside colour: ice blue) hosting the dichloromethane molecules viewed along the crystallographic a) *a* and b) *b* axis, respectively. The solvent molecules are omitted for the sake of clarity.

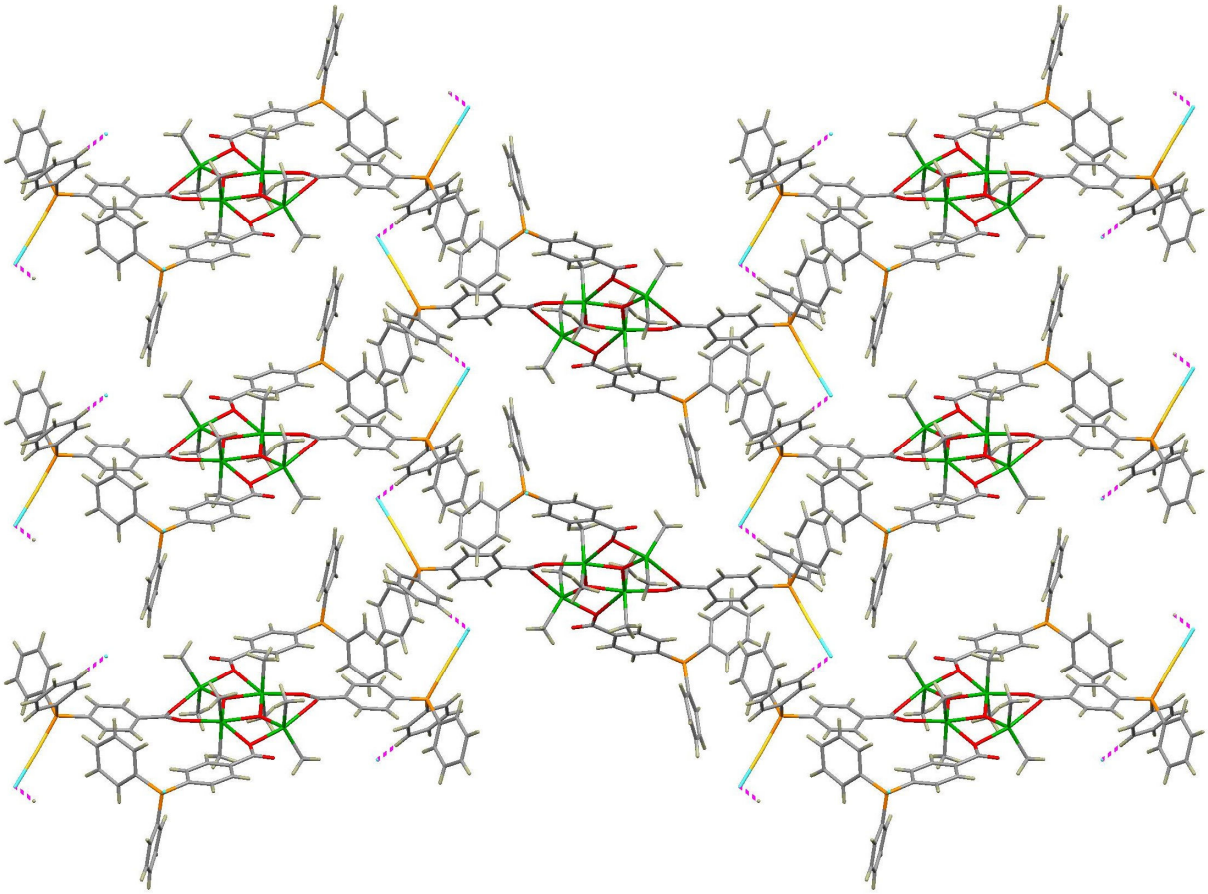

**Fig. S11** The crystal structure showing the brick-wall arrangement of **2** supported by C–H···Cl contacts* (dotted magenta lines) viewed along the crystallographic *a* axis. The solvent molecules are omitted for the sake of clarity.
*C(5D)–H(5D)···Cl(2)$^{i}$ 3.48(2) Å and 139.0°; *i* = 2–x, –1/2+y, 1/2–z.

## 4. Optical properties and computational studies

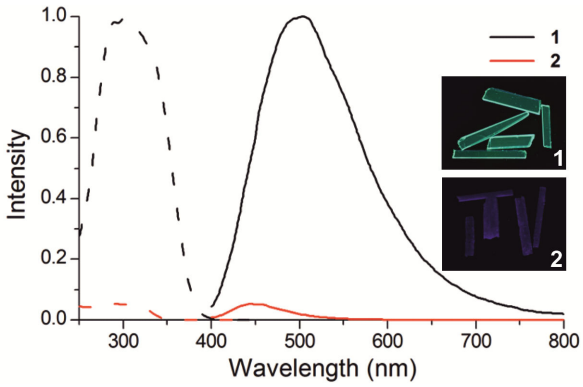


**Fig. S12** Emission (solid lines) and excitation (dashed lines) spectra of **1** (black lines) and **2** (red lines) at 298 K ($\lambda_{ex}$ = 312 nm). Inset shows photographs of **1** and **2** taken under 312 nm UV illumination.

**Table S3** Photophysical properties (luminescence maxima, quantum yields and lifetimes) of the Hdppba, **1** and **2**, respectively.

| Compound | $T$ (K) | $\lambda$ (nm) | $\Phi$ | $\tau$ (μs) |
|---|---|---|---|---|
| Hdppba | 298 | 490 | 0.22 | 0.0038 |
| | 77 | 500 | – | 0.0047 |
| **1** | 298 | 502 | 0.14 | 0.0042 |
| | 77 | 522 | – | 0.0062 |
| **2** | 298 | 447 | 0.008 | 6.7 |
| | 77 | 434 | – | 510 |

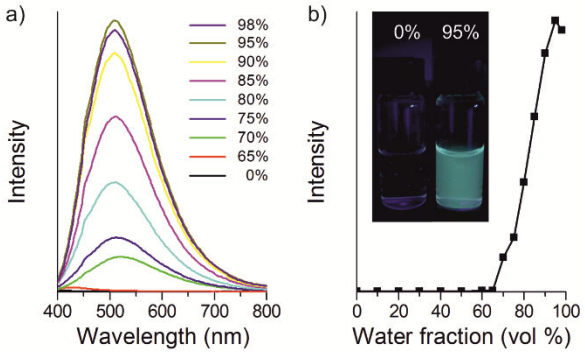


**Fig. S13** a) Emission spectra and b) plots of maximum emission intensity of metalloligand **1** versus water fraction in MeOH:$H_2O$ mixtures ($\lambda_{ex}$ = 312 nm; *c* = 10 μM). Inset: photograph of **1** in MeOH and 5:95 MeOH:$H_2O$ (%) mixture upon 312 nm UV lamp excitation.

To examine whether the metalloligand **1** displays *aggregation-induced emission* (AIE), its emission spectra in MeOH and MeOH:$H_2O$ solutions were recorded (Fig. S13). As expected, complex **1** is non-emissive when fully dissolved in good solvents such as methanol or dichloromethane, because of the non-radiative decay via the active intramolecular rotation of aromatic rings. As shown in Fig. S13, it remains practically non-emissive in mixed MeOH:$H_2O$ solutions with water content less than 70%, however, a bright green emission turns on upon further increasing the water content to 95%. The emission spectrum recorded in 5:95 of MeOH:$H_2O$ (%) mixture is centered at 507 nm with φ value of 0.06 when excited with 312 nm light. This markedly enhanced luminescence turn on upon molecular aggregation in MeOH:$H_2O$ solutions is also reflected by the changes in quantum yield values from 0% in methanol and 6% in 5:95 MeOH:$H_2O$ (%) mixture. These results show that this tetraorganostannoxan **1** exhibits AIE behaviour. To our knowledge, this is the first study on the AIE-activity of tetranuclear stannoxanic assemblies.

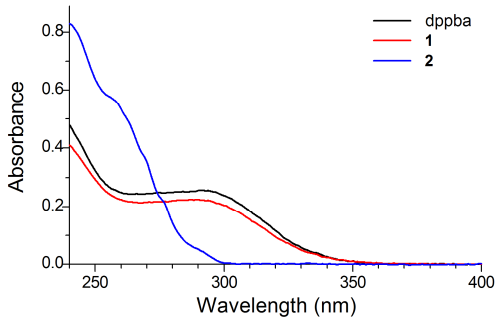


**Fig. S14** Absorption spectra of Hdppba (40 μM), **1** and **2** (10 μM) in $CH_2Cl_2$.

The absorption spectra of Hdppba and **1** in $CH_2Cl_2$ show intense bands at $\lambda$ = 294 nm and $\lambda$ = 290 nm whereas **2** exhibits only a structureless absorption continuum below $\lambda$ = 300 nm (Fig. S14).

Based on DFT calculations on the optimized singlet ground state structure of Hdppba and TD DFT analysis (Fig. S15) the intense absorption band can be attribute to transitions between the highest occupied molecular orbital and lowest unoccupied molecular orbital (HOMO → LUMO, $\lambda_{calc}$ = 301 nm, $f$ (oscillator strength) = 0.238; Table S4). The HOMO is dominated by the lone pair orbital of the phosphorus atom and LUMO located has major contribution coming from the carboxyphenyl part molecule (Fig. S16). Therefore the HOMO → LUMO transition tentatively attributed to intramolecular charge-transfer (ICT) transition involving promotion of an electron from the lone pair of the phosphorus atoms to empty π* orbital of carboxyphenyl part of the Hdppba ligand.

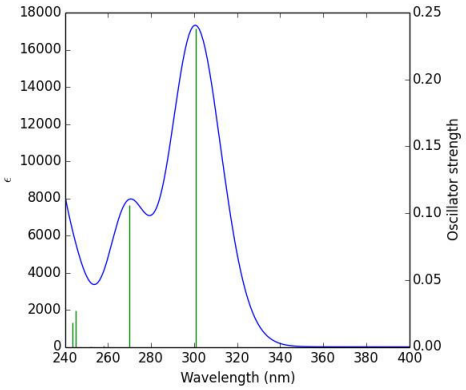


**Fig. S15** Simulated absorption spectrum of Hdppba ligand.

**Table S4** Absorption and emission wavelengths ($\lambda$), oscillator strengths ($f$) and orbital compositions for *optimized structure* of Hdppba ligand computed by TD DFT method (H = HOMO, L = LUMO).

| Exc. state | $\lambda$ (nm) | $f$ | Assignment |
|---|---|---|---|
| **$S_1$** | **300.7** | **0.2378** | **H→L (97%)** |
| $S_2$ | 269.9 | 0.1061 | H→L+1 (97%) |
| $S_3$ | 258.0 | 0.0008 | H→L+2 (61%), H–2→L (16%) |
| $S_4$ | 252.2 | 0.0002 | H–6→L (81%), H–7→L (11%) |
| $S_5$ | 245.0 | 0.0274 | H→L+3 (26%), H→L+2 (22%), H→L+5 (16%), H–4→L (10%) |
| $S_6$ | 243.5 | 0.0182 | H→L+3 (60%), H→L+5 (11%) |
| $S_7$ | 238.5 | 0.0062 | H–1→L (40%), H→L+4 (34%) |
| $S_8$ | 236.6 | 0.0148 | H–1→L (27%), H→L+4 (24%), H–2→L (22%) |
| $S_9$ | 234.2 | 0.0239 | H–2→L (35%), H–1→L (27%), H→L+4 (10%) |
| $S_{10}$ | 231.0 | 0.0375 | H–3→L (58%), H–4→L (25%) |

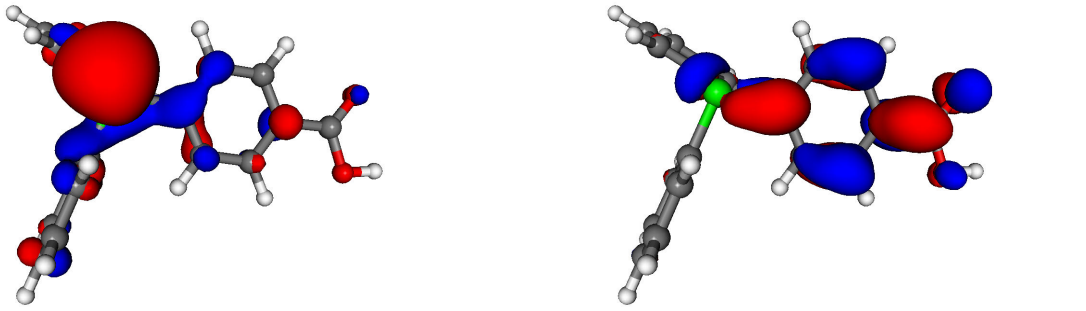

HOMO LUMO

**Fig. S16** Contour plots of the HOMO and LUMO superimposed on the optimized structure of Hdppba ligand.

The similar shape of the absorption spectra of Hdppba and **1** (Fig. S14) indicates that mainly the dppba responsible for the light absorption and no or very small interactions exist between the dppba and metal (Sn) atoms in **1**. According to the quantum chemical calculations, the lowest energy absorption band (at $\lambda$ = 294 nm) is assigned to the composition of the transitions ($\lambda_{calc}$ = 296 nm, $f$ (oscillator strength) = 0.477 and $\lambda_{calc}$ = 294 nm, $f$ (oscillator strength) = 0.985; Table S5) between the four highest occupied molecular orbitals (HOMO to HOMO–3) and the four lowest unoccupied molecular orbitals (LUMO to LUMO+3). The HOMOs are localized mainly on the the phosphorous atoms, whereas the LUMOs are located on the carboxyphenyl part of the dppba (Fig. S18). Thus, the main absorption band is tentatively attributed to intramolecular charge-transfer (ICT) transitions similar to dppba without any metal contribution.

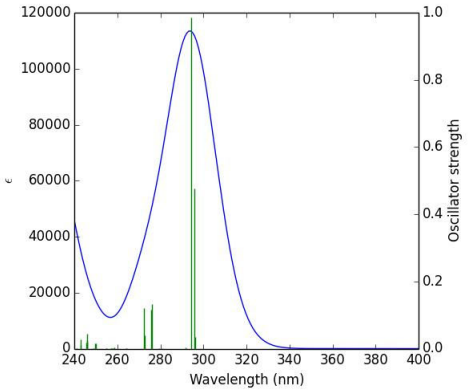


**Fig. S17** Simulated absorption spectrum of metalloligand **1**.

**Table S5** Absorption and emission wavelengths ($\lambda$), oscillator strengths ($f$) and orbital compositions for *optimized structure* of metalloligand **1** computed by TD DFT method (H = HOMO, L = LUMO).

| Exc. state | $\lambda$ (nm) | $f$ | Assignment |
|---|---|---|---|
| $S_1$ | 296.3 | 0.0338 | H–3→L (47%), H–1→L+2 (23%), H→L+3 (14%), H–2→L+1 (11%) |
| **$S_2$** | **295.8** | **0.4766** | **H–2→L+1 (60%), H–3→L (26%)** |
| **$S_3$** | **294.1** | **0.9848** | **H–1→L+2 (47%), H→L+3 (42%)** |
| $S_4$ | 291.7 | 0.0039 | H→L+3 (30%), H–1→L+2 (24%), H–2→L+1 (22%), H–3→L (18%) |
| $S_5$ | 280.8 | 0.0021 | H–1→L (98%) |
| $S_6$ | 279.6 | 0.0022 | H→L+1 (97%) |
| $S_7$ | 276.2 | 0.1331 | H–2→L+5 (96%) |
| $S_8$ | 275.8 | 0.1154 | H–3→L+4 (96%) |
| $S_9$ | 272.5 | 0.0385 | H–1→L+6 (89%) |
| $S_{10}$ | 272.4 | 0.1207 | H→L+7 (89%) |
| $S_{11}$ | 270.5 | 0.0000 | H→L (98%) |
| $S_{12}$ | 269.2 | 0.0000 | H–1→L+1 (99%) |
| $S_{13}$ | 264.2 | 0.0002 | H–3→L+2 (98%) |
| $S_{14}$ | 264.1 | 0.0001 | H–2→L+3 (98%) |
| $S_{15}$ | 263.1 | 0.0000 | H–2→L (99%) |
| $S_{16}$ | 261.4 | 0.0000 | H–3→L+1 (99%) |
| $S_{17}$ | 260.5 | 0.0000 | H→L+2 (99%) |
| $S_{18}$ | 260.0 | 0.0000 | H–1→L+3 (99%) |
| $S_{19}$ | 258.4 | 0.0024 | H–2→L+8 (45%), H–8→L+1 (11%), H–2→L+11 (11%) |
| $S_{20}$ | 258.4 | 0.0016 | H–3→L+9 (42%), H–9→L (14%), H–3→L+10 (11%) |

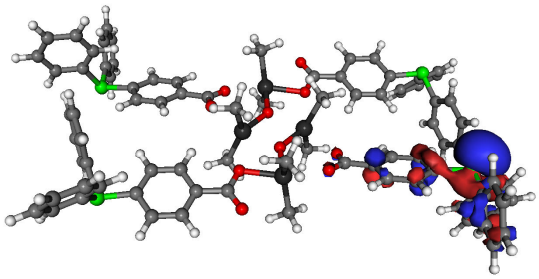

HOMO–3

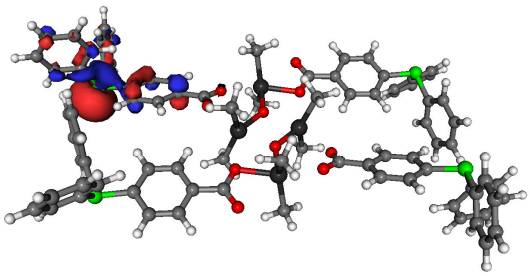

HOMO–2

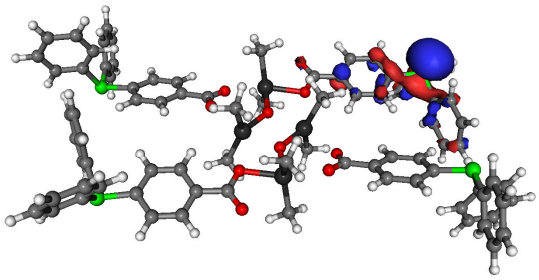

HOMO–1

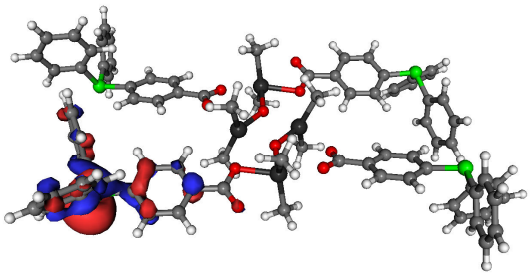

HOMO

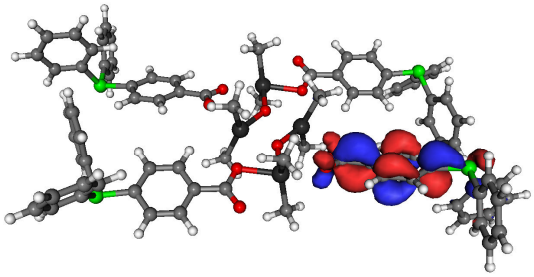

LUMO

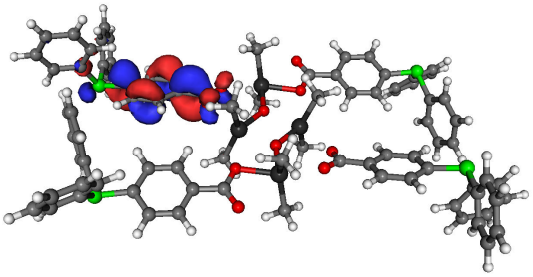

LUMO+1

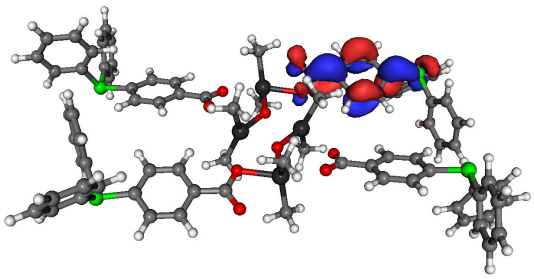

LUMO+2

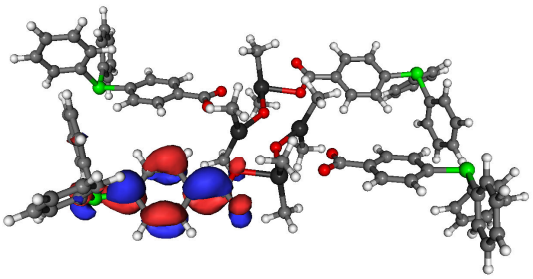

LUMO+3

**Fig. S18** Plots of selected molecular orbitals superimposed on the optimized structure of **1**.

In accordance with the TDDFT calculations (Fig. S19) the absorption spectrum of **2** is dominated by the electronic transitions from the ground state to the $S_{17}$ and $S_{25}$ ($\lambda_{calc}$ = 269 nm, *f* (oscillator strength) = 0.445 and $\lambda_{calc}$ = 263 nm, *f* (oscillator strength) = 0.554; Table S6) excited states. These excited states can be described by combinations of transitions between many occupied and unoccupied molecular orbitals. However all occupied orbitals are localized mainly on the chlorine and gold atoms while unoccupied orbitals are exclusively dominated by the phenyl rings connected to the carboxylate groups of the dppba ligands (Fig. S20).

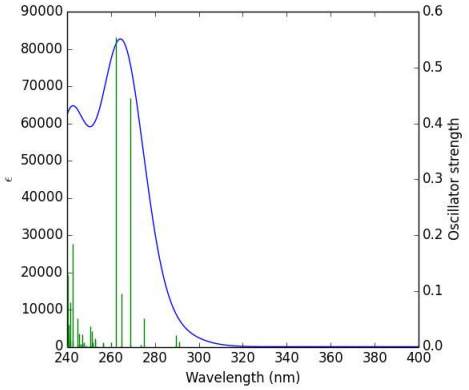


**Fig. S19** Simulated absorption spectrum of heterometallic **2**.

**Table S6** Absorption and emission wavelengths ($\lambda$), oscillator strengths ($f$) and orbital compositions for *optimized structure* of heterometallic **2** computed by TD DFT method (H = HOMO, L = LUMO).

| Exc. state | $\lambda$ (nm) | $f$ | Assignment |
|---|---|---|---|
| $S_1$ | 291.1 | 0.0098 | H→L+2 (44%), H→L+3 (39%) |
| $S_2$ | 291.1 | 0.0027 | H–1→L+2 (42%), H–1→L+3 (42%) |
| $S_3$ | 289.6 | 0.0204 | H–3→L+2 (41%), H–3→L+3 (39%) |
| $S_4$ | 289.5 | 0.0042 | H–2→L+3 (41%), H–2→L+2 (39%) |
| $S_5$ | 286.3 | 0.0000 | H→L (55%), H→L+1 (44%) |
| $S_6$ | 286.2 | 0.0000 | H–1→L (50%), H–1→L+1 (49%) |
| $S_7$ | 285.6 | 0.0000 | H–3→L (55%), H–3→L+1 (44%) |
| $S_8$ | 285.6 | 0.0000 | H–2→L (50%), H–2→L+1 (49%) |
| $S_9$ | 280.6 | 0.0000 | H–1→L+1 (50%), H–1→L (49%) |
| $S_{10}$ | 280.6 | 0.0000 | H→L+1 (55%), H→L (444%) |
| $S_{11}$ | 280.0 | 0.0000 | H–2→L+1 (50%), H–2→L (49%) |
| $S_{12}$ | 279.9 | 0.0000 | H–3→L+1 (55%), H–3→L (44%) |
| $S_{13}$ | 275.1 | 0.0505 | H–7→L+1 (38%), H–6→L (38%) |
| $S_{14}$ | 275.0 | 0.0027 | H–6→L+1 (40%), H–7→L (36%) |
| $S_{15}$ | 273.4 | 0.0034 | H–9→L (36%), H–9→L+1 (22%), H–8→L+1 (13%) |
| $S_{16}$ | 273.4 | 0.0017 | H–8→L (33%), H–8→L+1 (25%), H–9→L+1 (14%) |
| **$S_{17}$** | **268.8** | **0.4448** | **H–4→L+2 (36%), H–5→L+3 (34%)** |
| $S_{18}$ | 268.8 | 0.0043 | H–5→L+2 (36%), H–4→L+3 (33%) |
| $S_{19}$ | 264.8 | 0.0003 | H–1→L+2 (51%), H–1→L+3 (49%) |
| $S_{20}$ | 264.8 | 0.0003 | H→L+3 (51%), H→L+2 (48%) |
| $S_{21}$ | 264.8 | 0.0949 | H–5→L (26%), H–4→L+1 (24%) |
| $S_{22}$ | 264.7 | 0.0001 | H–4→L (28%), H–5→L+1 (26%) |
| $S_{23}$ | 264.3 | 0.0000 | H–2→L+2 (51%), H–1→L+3 (49%) |
| $S_{24}$ | 264.3 | 0.0000 | H–3→L+3 (52%), H–3→2 (48%) |
| **$S_{25}$** | **262.5** | **0.5537** | **H–13→L+1 (29%), H–12→L (29%)** |

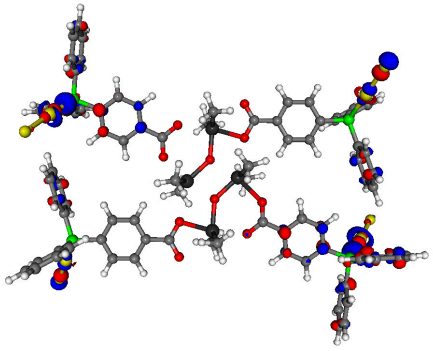

HOMO–13

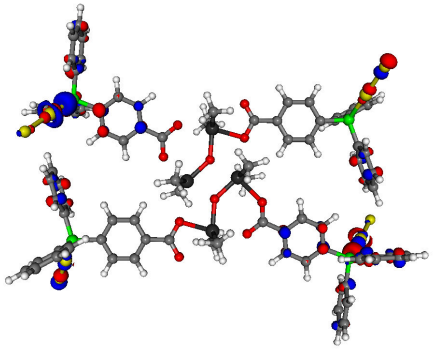

HOMO–12

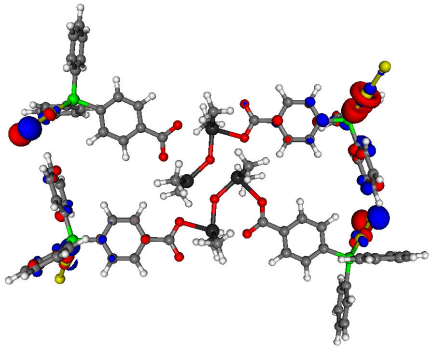

HOMO–5

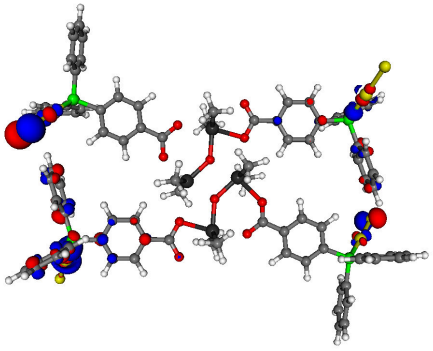

HOMO–4

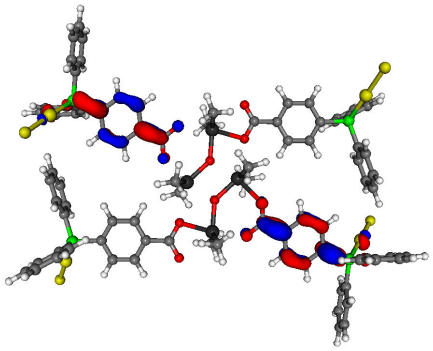

LUMO

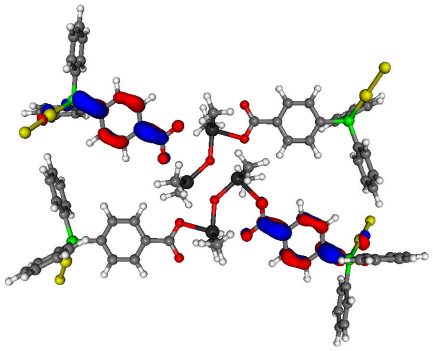

LUMO+1

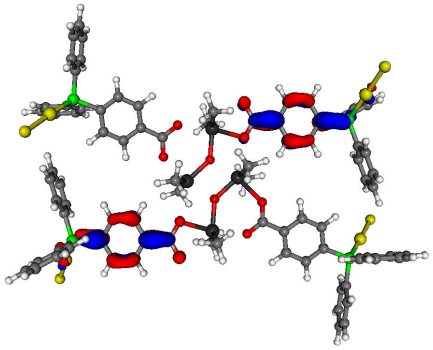

LUMO+2

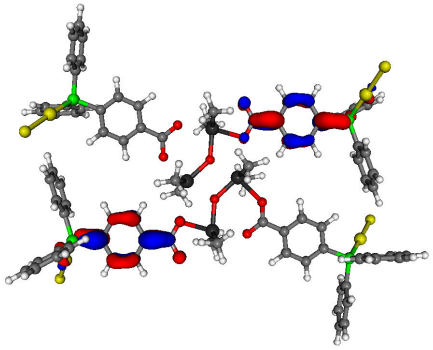

LUMO+3

**Fig. S20** Plots of selected molecular orbitals superimposed on the optimized structure of **2**.

## 5. Colorimetric response of crystals of 2 to different dye molecules

Freshly prepared crystals of **2** (10 mg) were placed in 1 mL saturated aqueous solution of dyes. During a period of 7 days, the supernatant solution was removed and replaced with fresh dye solution 10 times. After the seventh day of inclusion, the crystals were removed from solution and rinsed thoroughly with water. To assess the dye inclusion and uniformity, MR-rich and MB-rich crystals of **2** were sliced into pieces to visualize their inner portion. As shown in Fig. S21, the middle portion of both MR-rich and MB-rich crystals of **2** was coloured thoroughly by dyes. This uniform coloration suggests that the organic dye molecules deeply penetrate into the guest-accessible large pores instead of only adsorbing on the crystals' external surfaces.

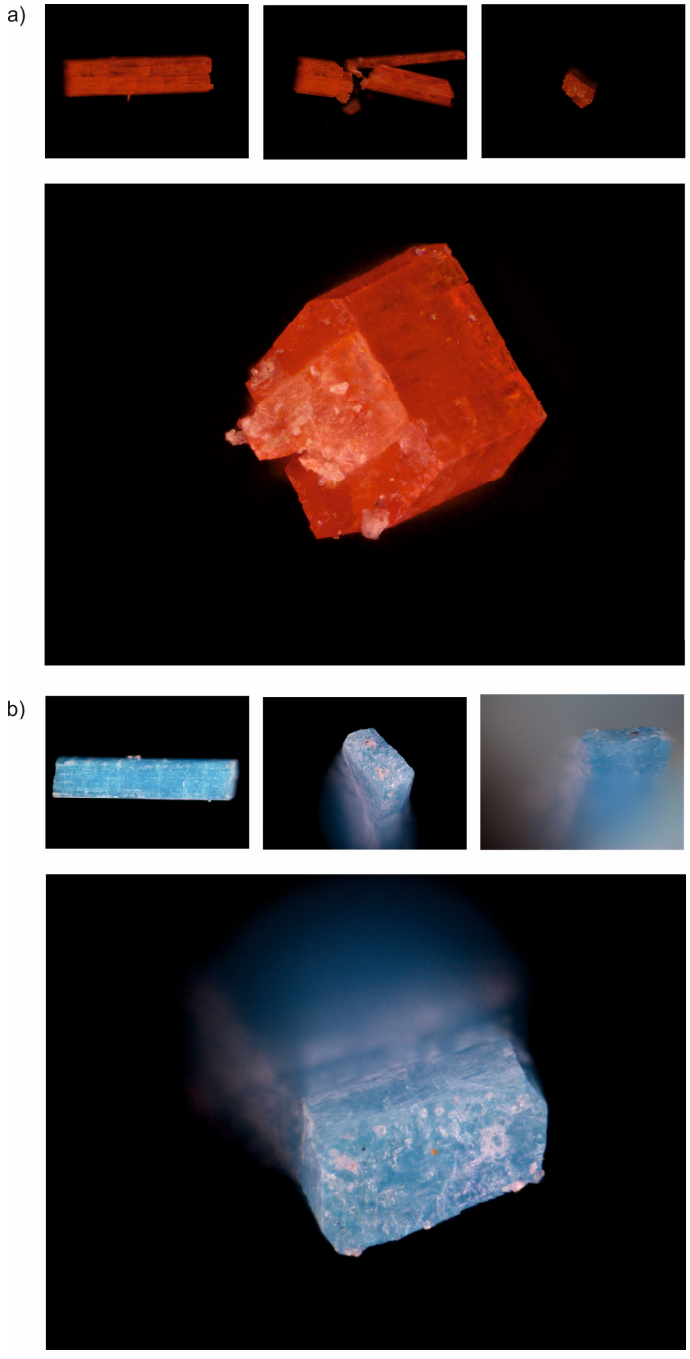


**Fig. S21** a) MR-rich and b) MB-rich crystals of **2** sliced into pieces.

Next, the dried dyed-crystals of **2** were precisely weighed with a micro balance and digested in 3 mL of methanol. The methanolic solution was quantitatively transferred to a 5 ml volumetric flask and methanol was added to obtain precise dilution. UV-Vis absorption spectroscopic analysis of the resulting solutions allowed for determination of the concentrations of the dyes and calculation of the adsorption capacity of **2**. The content of the included dye molecules in MR-rich and MB-rich **2** systems were determined by UV-VIS spectroscopy to be 1.5 and 2 mg/g, respectively.

As a control experiment, the freshly prepared crystals of **1** (10 mg) were placed in 1 mL saturated aqueous solution of MR, MB and MO dyes, respectively. During a period of 7 days, the supernatant solution was removed and replaced with fresh dye solution several times. After the seventh day of inclusion, the crystals were removed from solution and rinsed thoroughly with water. As shown in Fig. S22, the dye molecules were not included into the crystals of **1**.

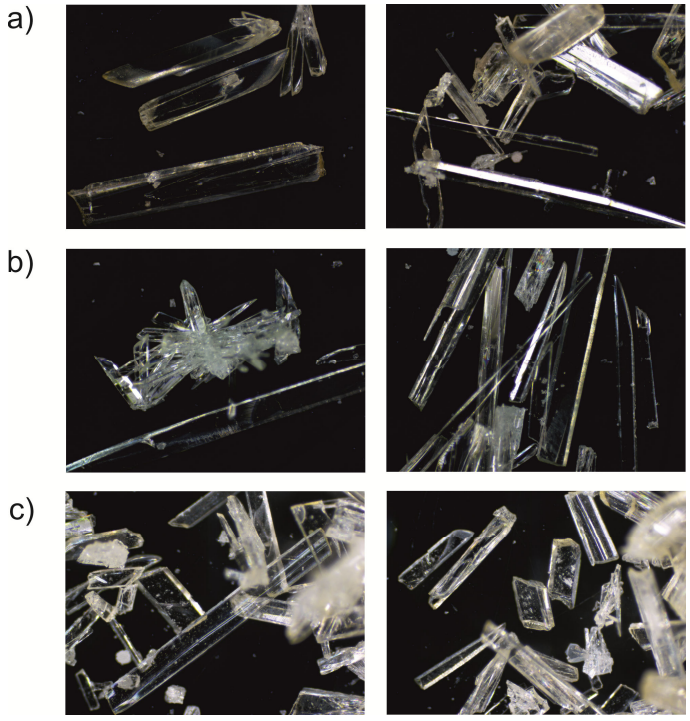


**Fig. S22** Crystals of **1** taken from aqueous a) MR, b) MB and c) MO dye solutions after a period of 7 days.

MR-rich solid **2**: $^{1}$H NMR (400 MHz, $CD_2Cl_2$, 25 °C): δ 8.06 (d, $J$ = 8.2 Hz, 8H), 7.63 – 7.48 (m, 48H), 0.98 (s, $^{2}J(^{119}Sn/^{117}Sn\text{-}^{1}H)$ = 87.0 Hz, 12H), 0.92 (s, $^{2}J(^{119}Sn/^{117}Sn\text{-}^{1}H)$ = 87.0 Hz, 12H)

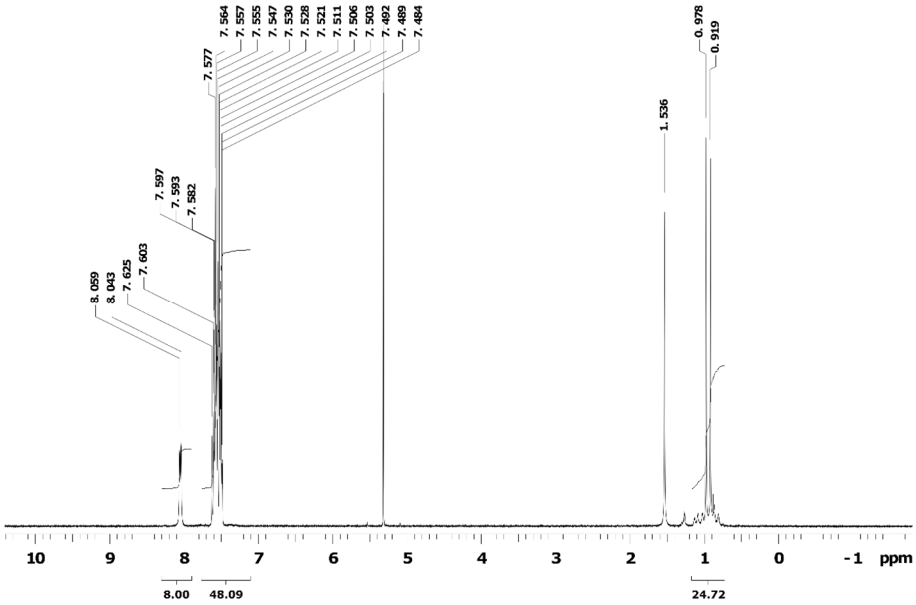


**Fig. S23** $^{1}$H-NMR spectrum of MR-rich solid **2**.

We used ESI MS experiments in the positive ionization mode to assess the amount of the included dyes in **2**. Complex **2**, dyes (MR and MB) and the dye-rich crystals of **2** were dissolved in dichloromethane then methanol was added to form a 1:2 solvent mixture. Powdered sample of **2** was dissolved to give a 0.1 mg/mL concentration, while a 0.05 mg/mL concentrated solution of dye-rich **2** was also prepared. The resolution of MS was set to 15000, and absolute intensity of ions at m/z 270.12 (for MR) and 284.12 (for MB) was monitored. Standard solutions were prepared by mixing aliquots of **2** with the appropriate amount of dye solution. The mass spectrum of dye-rich **2** was compared to mass spectrum of several standard solutions, which contained various amounts of dye in the range of $1.0 \cdot 10^{-3}$ to $3.5 \cdot 10^{-3}$ molar ratio. The mass spectrum of MR and MB dye-rich crystals of **2** is shown on Figures S24d and S25d, respectively. Figures S24b–c and S25b–c display the spectrum of standard solutions containing smaller and higher concentration of MR and MB dyes, respectively. From these measurements we can conclude that 1 mole of dye-rich crystals of **2** contains $2–3 \cdot 10^{-3}$ moles of dye (either MR or MB).

These values are in good agreement with the values determined by UV-Vis spectroscopy.

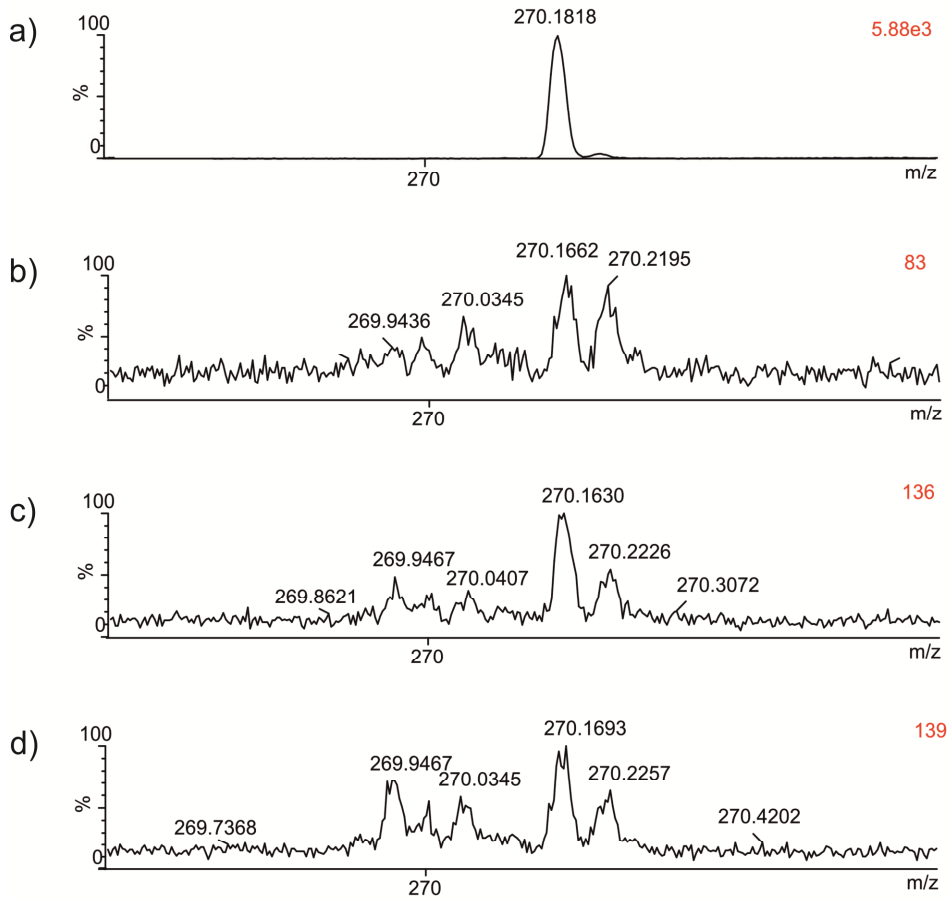


**Fig. S24** Molecular mass region of mass spectrum of a) MR, b) standard with $1.1 \cdot 10^{-3}$ mole ratio dye, c) standard with $3.3 \cdot 10^{-3}$ mole ratio dye and d) MR-rich **2**.

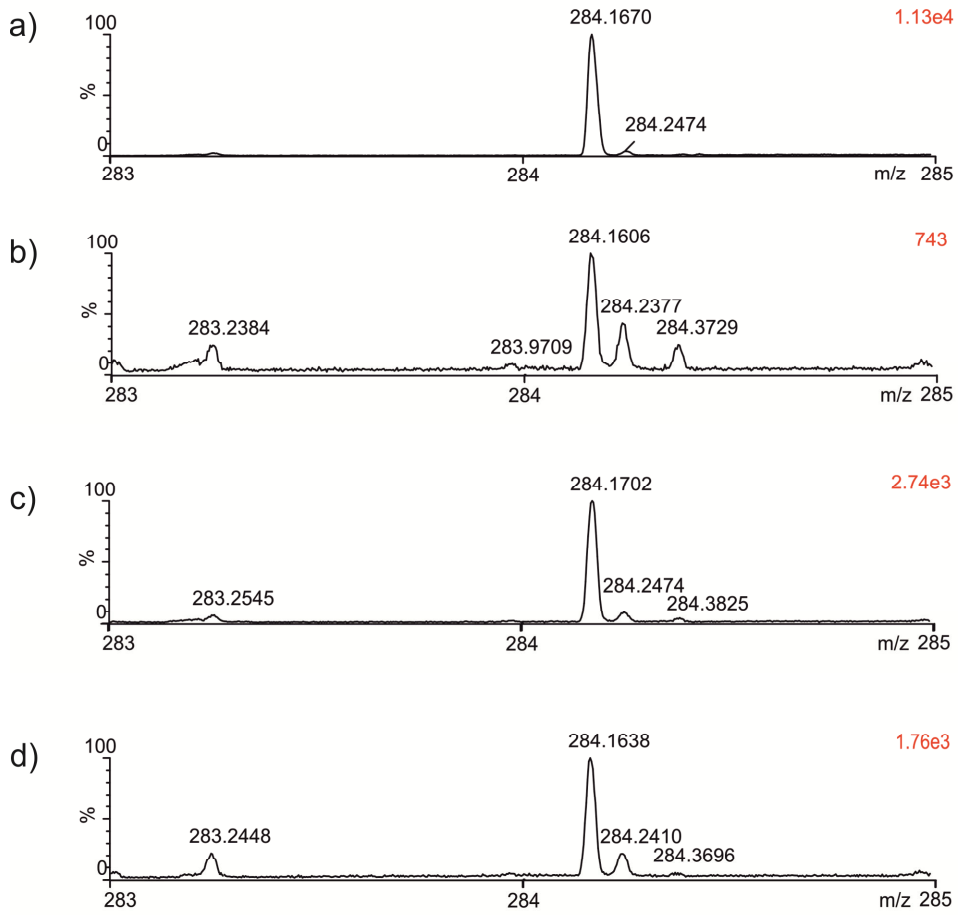


**Fig. S25** Molecular mass region of mass spectrum of a) MB, b) standard with $2.2 \cdot 10^{-3}$ mole ratio dye, c) standard with $2.8 \cdot 10^{-3}$ mole ratio dye and d) MB-rich **2**.

## 6. Colorimetric response of MR-rich solid 2 to acid/base vapours

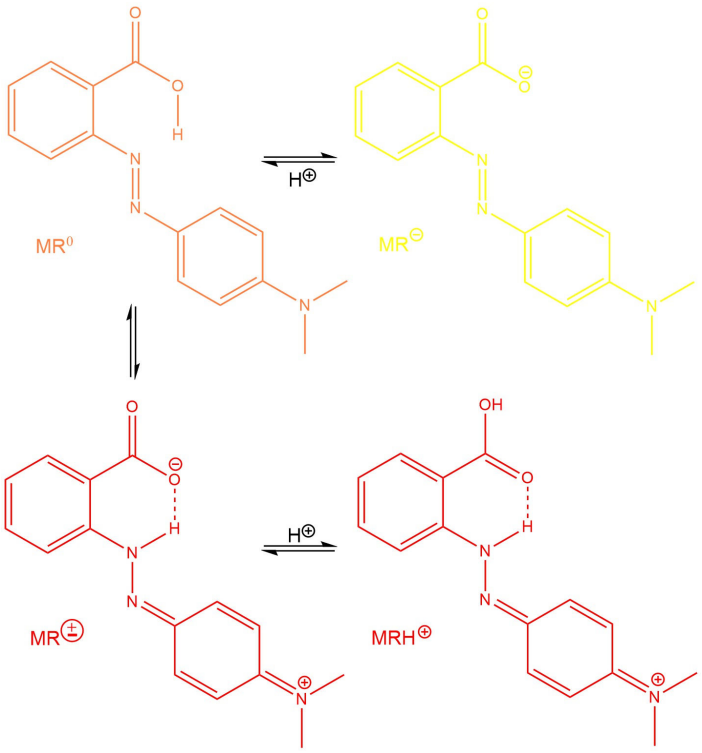


**Fig. S26** Four predominant species of pH-sensitive MR dye: neutral ($MR^0$), zwitterionic ($MR^{\pm}$), anionic ($MR^-$), and protonated ($MRH^+$), respectively.[9]

A vial containing the crystals of MR-rich **2** and a beaker containing drop of concentrated $NH_3$ solution were placed under a second larger beaker. The initial colour change from red to yellow occurred very quickly (within 1 minute), and after 3 minutes, no further colour change can be observed by the naked eye. When the source of $NH_3$ was removed, and the ambient air entered the vial, the crystal reverted back to red over the course of 1 hours. This reversion can be accelerated by using HCl (from concentrated HCl solution) or humid $CO_2$ (from sublimed dry ice) vapours.

For the optical pictures showing the colorimetric change of MR-rich **2** system during the *acid-base sensing process*, the individual red crystal (Fig. S25 a) was placed in a Petri dish on an angled microscope slide. 1 mL of concentrated $NH_3$ solution (Fig. S25 b and c) was then placed on the bottom (without being in contact with the sample) and was covered with a lid. When the source of $NH_3$ was removed, and the ambient air entered the vial, the crystal reverted back to red over the course of 1 hours (Fig. S25 e). This reversion can be accelerated by using HCl (Fig. 25) or humid $CO_2$ vapours (Fig. S26). The HCl atmosphere was sourced from a drop of concentrated HCl solution and $CO_2$ atmosphere from sublimed dry ice. The micrographs were taken through the Petri dish lid.


**Fig. S27** a) Optical microscope images of MR-rich **2** at selected time intervals during $NH_3$ sorption and desorption process. *a*) Red-coloured crystal MR-rich **2** prior to $NH_3$ exposure. Yellow crystal obtained after exposure of the red crystal to ammonia vapours for *b*) 3 min and *c*) 7 min. The crystal reverted back to red following removal of ammonia upon standing in ambient air for *d*) 30 min and *e*) 60 min.


**Fig. S28** a) Optical microscope images of MR-rich **2** at selected time intervals during $NH_3$ sorption and desorption process. *a*) Red-coloured crystal of MR-rich **2** prior to $NH_3$ exposure. *b*) Yellow crystal obtained after exposure of the red crystal to ammonia vapours for 3 min. Yellow crystal exposed to humid $CO_2$ (from sublimed dry ice) for *c*) 3 min, *d*) 10 min and *e*) 20 min reverted.

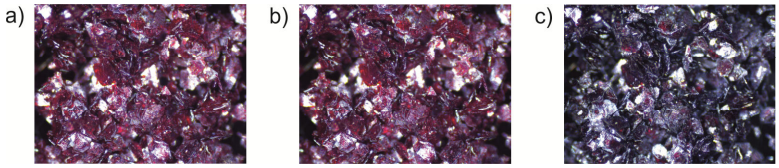


**Fig. S29** Optical microscope images of a) crystalline MR dye upon exposure to b) $NH_3$ and c) HCl vapours.

## 7. Luminescence response of 2 to guest molecules

A quartz plate (ca. 1 cm × 2 cm) deposited with a thin powder film of **2** was placed in a quartz fluorescence cell (1 cm × 1 cm). One drop of volatile guest such as aniline (AN), 3-fluoroaniline (FA), 4,*N*,*N*-trimethylaniline (TMA), *N*,*N*-dimethylaniline (DMA), *N*,*N*-diethylaniline (DEA) and 3,5-bis(trifluoromethyl)aniline (BTFMA) was placed in the cuvette, and then the system was closed. The emission intensity was monitored at regular time intervals. Relative intensity ($I/I_0$) was defined as the ratio of emission intensity ($I$) during volatile guest exposition and initial intensity ($I_0$) of **2** at monitoring wavelength.

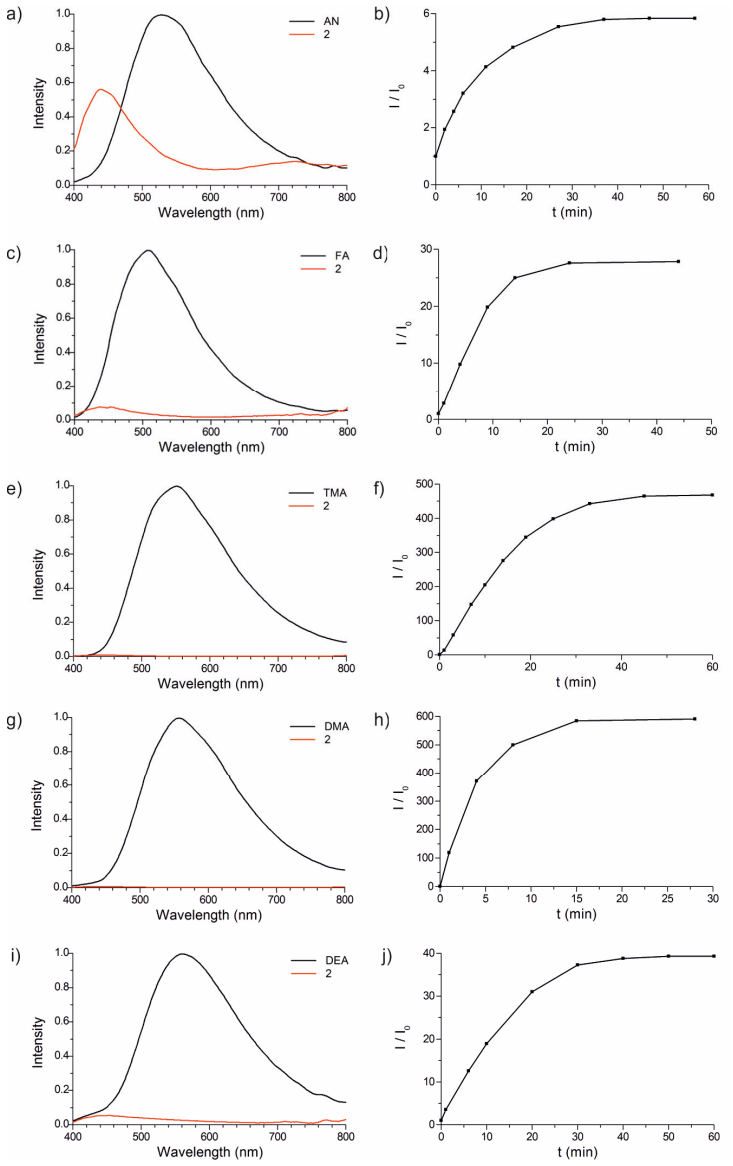


**Fig. S30** Luminescence turn on response of practically non-emissive crystalline **2** to aniline derivatives. Emission spectra of **2** and after exposure to a) AN, c) FA, e) TMA, g) DMA and i) DEA vapours. Time-dependent changes of emission intensity during b) AN, d) FA, f) TMA, h) DMA and j) DEA vapour exposure.

**Acknowledgements**

The authors gratefully acknowledge the support by MTA (Hungarian Academy of Sciences) through the Lendület Programme (LP2012-21/2012).

The authors are indebted to Márk Szabó for NMR spectroscopy, Dr. Tamás Holczbauer for single crystal X-ray diffraction measurements (Instrumentation Center, Research Centre for Natural Sciences, Hungarian Academy of Sciences, Budapest, Hungary) and for Mercury CSD 3.10 drawings[10] (Figs. S9 and S10). We also thank Dr. Szilvia Klébert (Institute of Materials and Environmental Chemistry, Plasma Chemistry Research Group, Research Centre for Natural Sciences, Hungarian Academy of Sciences, Budapest, Hungary) for gas sorption measurements and Dr. Olivér Ozohanics (MS Proteomics Research Group, Institute of Organic Chemistry, Research Centre for Natural Sciences, Hungarian Academy of Sciences, Budapest, Hungary) for HRMS-ESI measurements.

**References**

1. *Gaussian 09*, Revision C.01, M. J. Frisch, G. W. Trucks, H. B. Schlegel, G. E. Scuseria, M. A. Robb, J. R. Cheeseman, G. Scalmani, V. Barone, B. Mennucci, G. A. Petersson, H. Nakatsuji, M. Caricato, X. Li, H. P. Hratchian, A. F. Izmaylov, J. Bloino, G. Zheng, J. L. Sonnenberg, M. Hada, M. Ehara, K. Toyota, R. Fukuda, J. Hasegawa, M. Ishida, T. Nakajima, Y. Honda, O. Kitao, H. Nakai, T. Vreven, J. A. Montgomery, Jr., J. E. Peralta, F. Ogliaro, M. Bearpark, J. J. Heyd, E. Brothers, K. N. Kudin, V. N. Staroverov, R. Kobayashi, J. Normand, K. Raghavachari, A. Rendell, J. C. Burant, S. S. Iyengar, J. Tomasi, M. Cossi, N. Rega, J. M. Millam, M. Klene, J. E. Knox, J. B. Cross, V. Bakken, C. Adamo, J. Jaramillo, R. Gomperts, R. E. Stratmann, O. Yazyev, A. J. Austin, R. Cammi, C. Pomelli, J. W. Ochterski, R. L. Martin, K. Morokuma, V. G. Zakrzewski, G. A. Voth, P. Salvador, J. J. Dannenberg, S. Dapprich, A. D. Daniels, Ö. Farkas, J. B. Foresman, J. V. Ortiz, J. Cioslowski, and D. J. Fox, *Gaussian*, Inc., Wallingford CT, **2009**.
2. N. M. O'Boyle, A. L. Tenderholt, and K. M. Langner, *J. Comp. Chem.*, 2008, **29**, 839–845.
3. Ugo Varetto, Molekel 5.4, http://ugovaretto.github.io/molekel/
4. *a*) A. Deák, G. Tárkányi, *J. Organomet. Chem.*, 2006, **691**, 1693–1702; *b*) A. Deák and G. Tárkányi, in *Advances in Organometallic Chemistry Research*, ed. K. Yamamoto, Nova Science Publishers, Inc., New York, 2007, ch. 8, pp. 201–225.
5. V. Chandrasekhar, R. Suriya Narayanan and P. Thilagar, *Organomet.*, 2009, **28**, 5883–5888.
6. *a*) W. Li, D. Du, S. Liu, C. Zhu, A. M. Sakho, D. Zhu and L. Xu, *J. Organomet. Chem.*, 2010, **695**, 2153–2159; *b*) T. S. Basu Baul, W. Rynjah, E. Rivarola, A. Lyčka, M. Holčapek, R. Jirásko, D. de Vos, R. J. Butcher and A. Linden, *J. Organomet. Chem.*, 2006, **691**, 4850–4862.
7. A. Altomare, G. Cascarano, C. Giacovazzo, A. Guagliardi, M. C. Burla, G. Polidori and M. Camalli, *J. Appl. Cryst.*, 1994, **27**, 435.
8. G. M. Sheldrick, *Acta Cryst.*, 2015, **C71**, 3–8.
9. J. B. Benedict, D. E. Cohen, S. Lovell, A. L. Rohl and B. Kahr, *J. Am. Chem. Soc.*, 2006, **128**, 5548–5559.
10. C. F. Macrae, I. J. Bruno, J. A. Chisholm, P. R. Edgington, P. McCabe, E. Pidcock, L. Rodriguez-Monge, R. Taylor, J. van de Streek and P. A. Wood, *J. Appl. Cryst.*, 2008, **41**, 466–470.